



## ISTITUTO NAZIONALE DI RICERCA METROLOGICA Repository Istituzionale

A quantum resistance memristor for an intrinsically traceable International System of Units standard

*Original*

A quantum resistance memristor for an intrinsically traceable International System of Units standard / Milano, Gianluca; Zheng, Xin; Michieletti, Fabio; Leonetti, Giuseppe; Caballero, Gabriel; Oztoprak, Ilker; Boarino, Luca; Bozat, Özgür; Callegaro, Luca; De Leo, Natascia; Godinho, Isabel; Granados, Daniel; Koymen, Itir; Menghini, Mariela; Miranda, Enrique; Ribeiro, Luís; Ricciardi, Carlo; Suñe, Jordi; Cabral, Vitor; Valov, Ilia. - In: NATURE NANOTECHNOLOGY. - ISSN 1748-3387. - 20:12(2025), pp. 1884-1890.

<https://doi.org/10.1038/s41565-025-02037-5>

This version is available at: 11696/88380 since: 2026-02-27T08:14:07Z

*Publisher:*

NATURE PUBLISHING GROUP

*Published*

DOI:10.1038/s41565-025-02037-5

*Terms of use:*

This article is made available under terms and conditions as specified in the corresponding bibliographic description in the repository

*Publisher copyright*

(Article begins on next page)

# A quantum resistance memristor for an intrinsically traceable International System of Units standard

Received: 7 January 2025

Accepted: 15 September 2025

Published online: 27 October 2025

 Check for updates

Gianluca Milano <sup>1</sup>✉, Xin Zheng <sup>2</sup>, Fabio Michieletti <sup>3</sup>, Giuseppe Leonetti <sup>1,3</sup>, Gabriel Caballero<sup>4,5</sup>, Ilker Oztoprak <sup>6</sup>, Luca Boarino<sup>1</sup>, Özgür Bozat <sup>7</sup>, Luca Callegaro <sup>8</sup>, Natascia De Leo<sup>1</sup>, Isabel Godinho <sup>9</sup>, Daniel Granados <sup>4</sup>, Itir Koymen <sup>7,10</sup>, Mariela Menghini <sup>4</sup>, Enrique Miranda<sup>11</sup>, Luís Ribeiro<sup>9</sup>, Carlo Ricciardi <sup>3</sup>, Jordi Suñe <sup>11</sup>, Vitor Cabral <sup>9</sup>✉ & Ilia Valov <sup>2,12</sup>✉

The recent revision of the International System of Units (SI)—which fixed the numerical values of nature’s fundamental constants—has opened new perspectives for practical realizations of SI units. Here we demonstrate an intrinsic resistance standard based on memristive nanoionic cells that operate in air at room temperature and are directly accessible to end users. By driving these devices into the quantum conductance regime and using an electrochemical-polishing-based programming strategy, we achieved quantum conductance levels that can be exploited as intrinsic standard values. An interlaboratory comparison confirmed metrological consistency, with deviations of  $-3.8\%$  and  $0.6\%$  from the agreed SI values for the fundamental quantum of conductance,  $G_0$ , and  $2G_0$ , respectively. These results lay the groundwork for the implementation of national metrology institute services on chip and for the development of self-calibrating measurement systems with zero-chain traceability.

Guaranteeing reliability and accuracy of measurements in all spheres of human knowledge is of ultimate priority to ensure the proper function of science and technology, and for the comfort and quality of our daily activities. To comply with this objective, national metrology institutes (NMIs) realize, develop and maintain primary standards of measurement units. The revision of the International System of Units (SI) in 2019<sup>1,2</sup> represented a historic change of paradigm for metrology, opening a new perspective on the mise en pratique of the SI base

units. Indeed, SI units are now mainly defined in terms of fundamental constants of nature defined by fixed numerical values. These fixed values are exact with zero uncertainty, and therefore no longer need to be measured. Accordingly, any experiment able to correlate measurable physical quantities to a fundamental constant, or a set of fundamental constants, fixed by the SI becomes a direct realization of the corresponding SI unit. This new paradigm is expected to revolutionize metrology as the science of measurement, making it possible to bring

<sup>1</sup>Advanced Materials Metrology and Life Sciences Division, INRiM (Istituto Nazionale di Ricerca Metrologica), Turin, Italy. <sup>2</sup>Forschungszentrum Jülich, Peter Grünberg Institute (PGI-7), Jülich, Germany. <sup>3</sup>Department of Applied Science and Technology, Politecnico di Torino, Turin, Italy. <sup>4</sup>IMDEA Nanociencia, Cantoblanco, Madrid, Spain. <sup>5</sup>Facultad de Ciencias Físicas, Universidad Complutense de Madrid, Madrid, Spain. <sup>6</sup>Department of Physics, Gebze Technical University, Gebze, Kocaeli, Turkey. <sup>7</sup>TUBITAK National Metrology Institute (UME), Gebze, Turkey. <sup>8</sup>Quantum Metrology and Nanotechnologies Division, INRiM (Istituto Nazionale di Ricerca Metrologica), Turin, Italy. <sup>9</sup>Instituto Português da Qualidade, Caparica, Portugal. <sup>10</sup>Department of Electrical and Electronics Engineering, TOBB University of Economics and Technology, Ankara, Turkey. <sup>11</sup>Departament d’Enginyeria Electrònica, Universitat Autònoma de Barcelona, Cerdanyola del Valles, Spain. <sup>12</sup>Institute of Electrochemistry and Energy Systems, Bulgarian Academy of Sciences (BAS), Sofia, Bulgaria. ✉e-mail: [g.milano@inrim.it](mailto:g.milano@inrim.it); [vcabral@ipq.pt](mailto:vcabral@ipq.pt); [i.valov@fz-juelich.de](mailto:i.valov@fz-juelich.de)

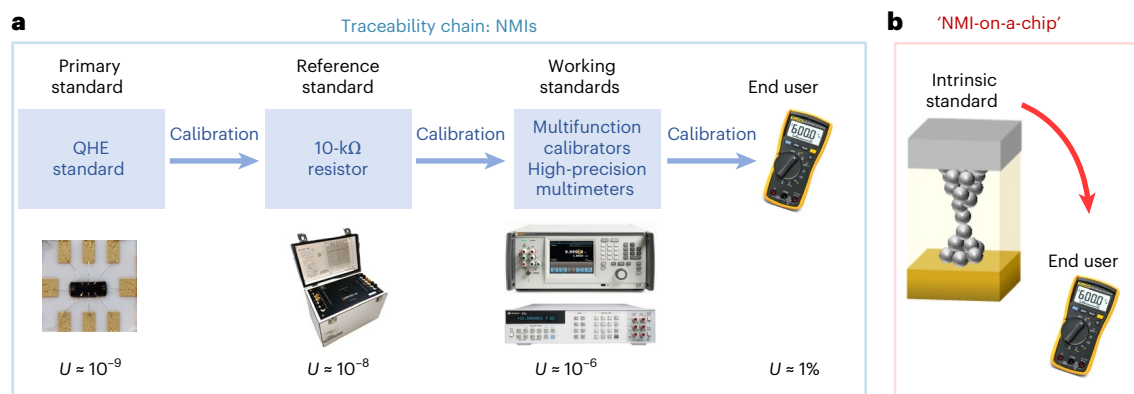


**Fig. 1 | NMI on-a-chip.** **a**, Conventional traceability chain for electrical resistance measurements. The chain starts with a comparison of the primary standard based on QHE with a first-level standard resistor (10 kΩ in the example given). In the second step of the traceability chain, this resistor standard is used to calibrate a second-order level of working standards as high-accuracy multifunction calibrators or digital multimeters. At the end of the chain, working standards are exploited to calibrate end-user equipment. Each step of the chain results in an increase of the measurement relative uncertainty  $U$ . The relative uncertainty

$U$  for the 10-kΩ example goes from some parts in  $10^9$  (the uncertainty related to the limitations in the practical implementation of the quantum Hall resistance values) to some parts in  $10^6$  (the typical specifications of precise multifunction calibrators or digital multimeters in the 10-kΩ range). At the end of the chain, we can find, for example, a hand-user multimeter with an accuracy specification of the order of 1%. **b**, Implementation of the memristive intrinsic standard of resistance directly in the end-user equipment, bringing NMI services on chip and allowing the realization of self-calibrating systems with zero-chain traceability.

measurement technology and metrology out of NMIs directly to the end-user. In particular, the miniaturization and integration of NMI services on chip (for example, the NIST on a Chip programme<sup>3</sup>) working according to the principles of quantum physics can enable the realization of reliable SI-traceable self-referenced systems. In the field of electrical metrology, quantum phenomena such as the quantum Hall effect, the Josephson effect and single-electron transport effect have been widely explored for the practical realization of resistance, voltage and current electrical units, respectively<sup>4</sup>. Despite the recognized performances of metrological devices based on these quantum phenomena, the involved large size experimental set-ups and complexity of related measurements limit their realization almost exclusively to universities and metrology institutions. In the framework of the SI, the fundamental quantum of conductance,  $G_0$ , is a quantity having a fixed numerical value with zero uncertainty (Supplementary Section 1). Hence, an experiment or device exhibiting a physical observable related to  $G_0$  can be exploited as a standard of resistance. Although it has been suggested that quantum effects in memristive devices could be exploited to overcome the main issues related to on chip integration of electrical standards<sup>5</sup>, an experimental verification is still missing. While several approaches have been followed to obtain quantum conductance levels in memristive devices<sup>6–28</sup>, their practical application has been hindered by a lack of substantial progress in programming and controlling such quantum levels.

In this Article, we report on a programmable resistance standard based on nanoionic memristive devices working in air, at room temperature, and implementable on chip. Besides introducing the electrochemical polishing effect to achieve reliable quantum conductance levels as multiples of  $G_0$ , we provide a programming strategy that enables practical exploitation of quantum conductance effects even in presence of variability. Based on the results from an interlaboratory comparison involving three NMIs and three academic/research centres, we established consensus values of conductance states related to  $G_0$  and  $2G_0$  that deviates from SI values by  $-3.8\%$  and  $0.6\%$ , respectively. These results establish the basis for the realization of self-calibrating systems embedding intrinsic standards directly traceable to the SI.

## NMI services on chip

Metrological traceability is a fundamental requirement for any measurement process and is at the base of the intercomparability and validity of measurement outcomes, an essential need in science and in our daily

activities. Traceability is defined as a property of a measurement result whereby the result can be related to a reference standard through a documented unbroken chain of calibrations, each calibration contributing to the overall measurement uncertainty<sup>29</sup>. In this framework, a chain of calibrations (or traceability chain) ensures the link between a common established reference (which underpins the comparability of measurement results) at the top of the chain and the measurement result given by an instrument on a lower step along the chain. Uncertainty increases after every step of the chain as the result of the contribution of the uncertainty associated with a new measurement that relates the instrument under calibration with the reference standard corresponding to that step.

Figure 1a shows an example of the conventional traceability chain for electrical resistance measurements. The reference standard for resistance based on the quantum Hall effect (QHE) (the standard having the highest metrological properties<sup>30,31</sup>) has been established for decades and is based on the von Klitzing constant  $R_K$  (ref. 32). Notably, the potential use of the quantum anomalous Hall effect in metrology, which enables the realization of a resistance standard operating at zero external magnetic field, but still at cryogenic temperatures ( $\sim 35$  mK) and vacuum conditions, has recently been demonstrated<sup>33</sup>. The traceability chain relies on a comparison of the primary standard based on the QHE with a first-level standard resistor that is then used to calibrate a second-order level of working standards such as multifunction calibrators or digital multimeters. Each step of the chain results in an increase of the measurement uncertainty  $U$  and, at the end of the chain, we can find, for example, a hand-user multimeter with a specification of the order of 1%. Each calibration in the traceability chain must be periodically repeated due to possible drifts of each measurement standard caused by operating time, environmental conditions and/or use. This means cost, long periods of unavailability of the measurement equipment and a lot of effort in the management process. Moreover, the QHE primary method has expensive and complex systems with highly demanding operating conditions because it needs to operate in vacuum conditions, at very low temperatures ( $\sim 1$  K) and under high applied magnetic fields (6–12 T) (Supplementary Section 2).

Memristive nanoionic devices, showing quantum conductance levels that are multiples of the fundamental quantum of conductance in air, at room temperature and implementable on chip, are therefore ideal candidates to be exploited as intrinsic standards of resistance. In this context, memristive devices make it possible to have an ‘NMI

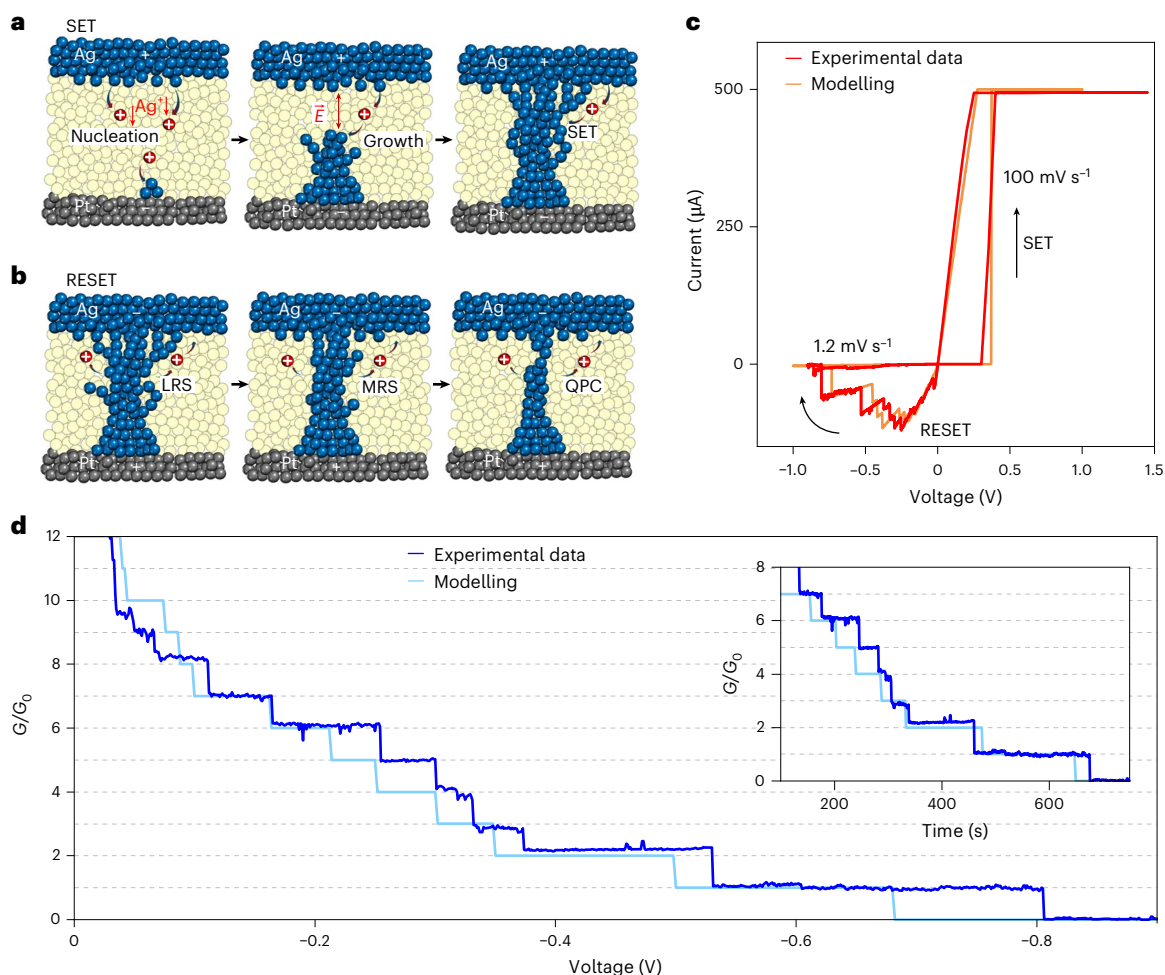


**Fig. 2 | Quantum conductance levels stabilized by electrochemical polishing.**

**a**, Schematic representation of the SET process in a memristive cell, that is, an electrochemically driven process additionally accelerated by the electric field formed at the tip apex. The harsh conditions during filament growth in these nanoscale devices, characterized by extremely high current densities exceeding  $10^8 \text{ A cm}^{-2}$  in conditions of high electric field acceleration ( $>10^8 \text{ V cm}^{-1}$ ), typically led to high unpredictability and variability of quantum conductance levels. **b**, The electrochemical polishing effect makes it possible to obtain more reliable quantum conductance levels by removing/dissolving first the unstable atoms at the contact configuration during the RESET process, but keeping the more

stable ones. In this framework, the system evolves through discrete levels of conductance from a low-resistance state (LRS) to an intermediate metastable-resistance state (MRS) to a QPC. **c**, Example of a cycle showing abrupt SET obtained through a voltage sweep rate of  $100 \text{ mV s}^{-1}$  and RESET with discrete levels obtained by electrochemical polishing through a slow voltage sweep ( $1.2 \text{ mV s}^{-1}$ ). **d**, The RESET process obtained through electrochemical polishing shows stable quantum conductance plateaus that are multiples of  $G_0$ . Inset: the stability over time of the quantum conductance plateaus while sweeping the applied voltage.

on chip' available where the above-described traceability chain is no longer required (zero-chain traceability, Supplementary Section 3), enabling the realization of systems embedding the intrinsic standard that do not require any calibration (self-calibrating systems) (Fig. 1b).

### Electrochemical polishing in memristive devices

Redox-based memristive devices are two-terminal nanoionics devices in which an ion-conductive (switching) film is sandwiched between two metal electrodes. The operation principle and functionalities of these cells rely on resistive switching effects related to the formation and rupture of a nanosized conductive filament within thin films (typically oxides or other chalcogenides) under the action of an electric field<sup>34</sup>. As a consequence of the progressive growth of the nanosized metallic whisker, quantum point contacts (QPCs) have been reported for short circuit conditions. The latter are typically achieved during the SET process (that is, the process that turns the device from an high-resistance state to a low-resistance state; Supplementary Section 4)<sup>6,7,9</sup>, which is electrochemically driven, but it is characterized by extremely high current densities and high electric fields (Fig. 2a). The electric field

even increases during operation, due to the exponentially reducing distance between the tip apex and the electrode surface during the filament growth, until metallic contact is reached. Due to these extreme conditions, it is practically very difficult to control the filament growth process, resulting in large stochasticity in the shape, number of small dendrites/needles and the effective area of the formed contact. Accordingly, formation of QPCs is highly unpredictable and rather large filament(s) are formed under these harsh conditions. As a result, QPCs formed during the SET process largely vary in resistance value, and/or are highly unstable, even if formed at low voltages and currents. Alternatively, we propose forming QPCs during the RESET process (that is, the process that turns the device from a low-resistance state to a high-resistance state) in Ag/SiO<sub>2</sub>/Pt devices (Methods; details of materials and device configuration are given in Supplementary Section 5), exploiting the effect of electrochemical polishing (Supplementary Section 6). To obtain reliable QPC during RESET operation, after the SET process where a large filament is formed, we applied a sequence of voltages high enough to oxidize/dissolve the energetically unstable atoms in the filament and the peripheral nanoneedles in the contact

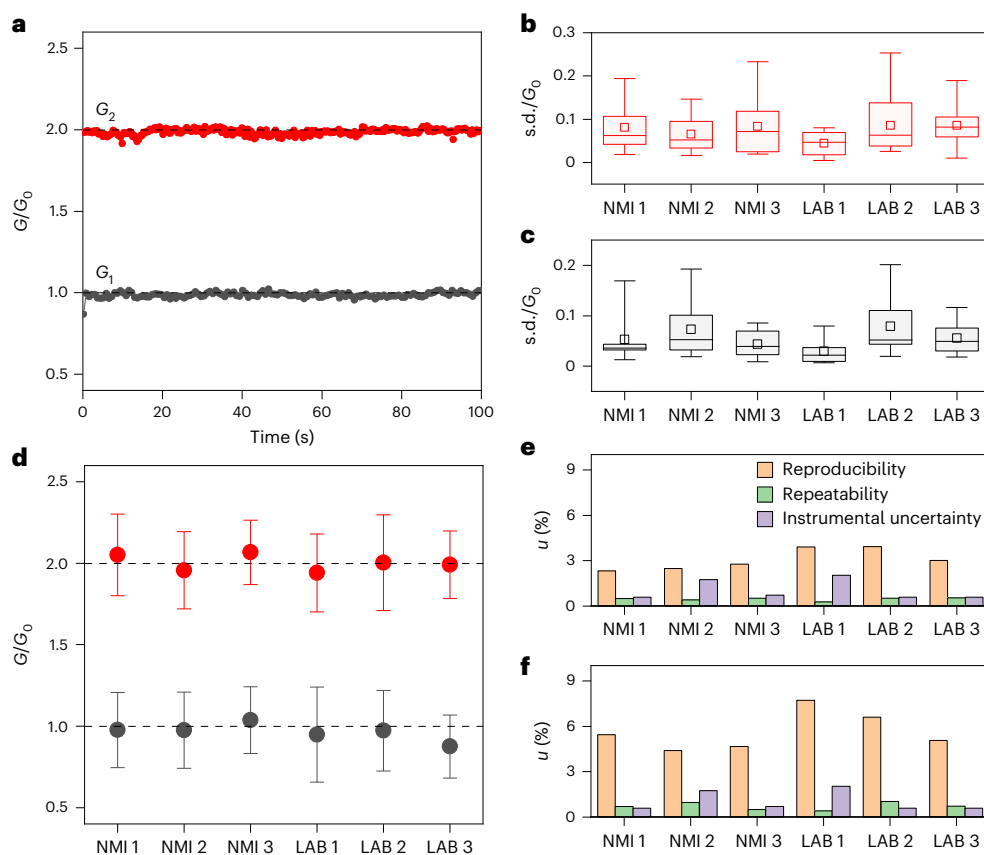


**Fig. 3 | Quantum conductance levels and uncertainty budget.** **a**, Stability of  $G_1$  and  $G_2$  quantum conductance levels achieved through a program-and-verify strategy in air and at room temperature. **b, c**, Repeatability of conductance values for  $G_2$  (**b**) and  $G_1$  (**c**), evaluated in terms of the s.d. over consecutive measurements of the programmed quantum levels, for the different NMIs and academic/research laboratories (LABs) participating in the interlaboratory comparison (see ‘Interlaboratory comparison’ in Methods for explanation of abbreviations). The sample size ( $N$ , the number of s.d. values for each participant) and the number of different devices used are presented in Supplementary Section 16. **d**, Reproducibility of conductance values for all participants in terms of the mean value of  $N$  mean values; the error bar represents the corresponding s.d. for  $G_1$  and  $G_2$ . The sample size ( $N$ , the number of mean values) and the number of different devices used are presented in Supplementary Section 16. **e, f**, Relative standard uncertainty components of  $G_2$  (**e**) and  $G_1$  (**f**), related to reproducibility, repeatability and instrumental uncertainty for each participant.

In box-plots, the midline represents the median of the  $N$  s.d. values, boxes show the 25th and 75th percentiles, and whiskers are the 5th and 90th percentiles. **d**, Reproducibility of conductance values for all participants in terms of the mean value of  $N$  mean values; the error bar represents the corresponding s.d. for  $G_1$  and  $G_2$ . The sample size ( $N$ , the number of mean values) and the number of different devices used are presented in Supplementary Section 16. **e, f**, Relative standard uncertainty components of  $G_2$  (**e**) and  $G_1$  (**f**), related to reproducibility, repeatability and instrumental uncertainty for each participant.

configuration, but at the same time sufficiently low not to remove the more stable core atoms (Fig. 2b). Using this approach, despite Joule heating effects, we avoid high Faradaic currents and electric field acceleration of ionic reactions and transport, which ultimately results in more reproducible and reliable QPCs. During the partial RESET process, we neither break the contact, nor dissolve the filament entirely, but the filament is progressively narrowed, achieving  $G < 10G_0$ , opposite to the abrupt SET process (Fig. 2c). In the partial RESET regime, the stepwise conductance changes correspond to integer multiples of  $G_0$  (Fig. 2d). Importantly, the quantum conductance states prepared by electrochemical polishing remain stable for several tens of seconds even under increasing negative voltage (Fig. 2d, inset), demonstrating a much higher stability and reliability compared with the QPC reached during the SET process. Thus, electrochemical polishing allows for predictable adjustment of stable quantum point levels, as required for the development of a quantum-based standard of resistance. A detailed discussion on the effect of electrochemical polishing in memristive devices can be found in Supplementary Section 7. It is worth remarking that the electrochemical polishing effect is best suited for memristive devices relying on the electrochemical metallization mechanism (ECM), as in our case (see Supplementary Section 8 for details).

Based on the electropolishing approach which aimed to slow RESET transitions, a stochastic model that considers conductance jumps  $\sim G_0$  accelerated by temperature (local power dissipation) and

not by the electric field is proposed (Methods and Supplementary Section 9). This is related to the fact that redox dynamics and/or out-diffusion of metallic species that control the filament dissolution are sufficiently suppressed during the RESET process. As can be observed in Fig. 2c,d, the behavioural model results nicely track the experimental data (additional data in Supplementary Section 10).

### Interlaboratory comparison

An interlaboratory comparison study involving three NMIs and three academic/research laboratories was carried out with the purpose of measuring the achieved quantum reference values (see Methods for details). This activity included the establishment of a measurement protocol and data processing according to international standards and well-recognized best practices<sup>35–37</sup>. The measurement protocol was based on a ‘program-and-verify’ approach that aimed to generate and sustain the desired quantum conductance reference levels, making it possible to exploit memristive devices as a quantum standard of resistance while dealing with conductance fluctuations. This approach consists of selecting the desired discrete quantum conductance level during the gradual step-like RESET obtained through electrochemical polishing, and subsequent evaluation of the conductance level to be used as reference value by means of a constant applied voltage that, at the same time, sustains the conductance state (Extended Data Fig. 1). This applied read voltage is expected to stabilize the quantum conductance state

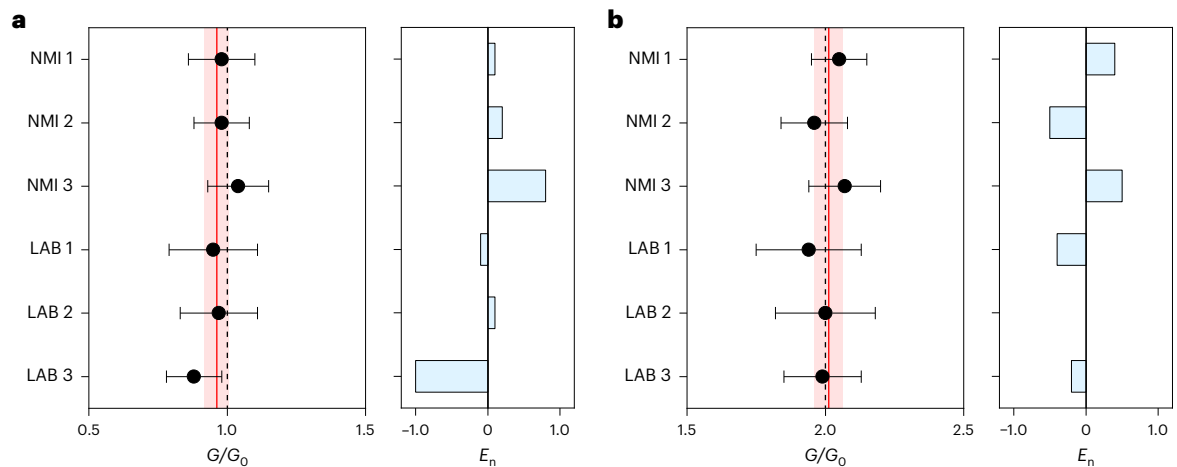


**Fig. 4 | Resistance standard.** **a, b**, Mean values of resistance standards based on memristive devices and corresponding expanded uncertainty (error bars) evaluated in different NMIs and laboratories (LABs) for  $G_1$  (**a**, left) and  $G_2$  (**b**, left). The red line is the consensus value  $G_{\text{cons}}$  of the participant's results, the

red shading is the corresponding expanded uncertainty  $U(G_{\text{cons}})$ , and the black dashed line shows the  $G_0$  and  $2G_0$  SI values. Right: the normalized error  $E_n$  of each participant exploited to qualify results with respect to the consensus value.

by exerting quantum pressure forces due to recoil of flowing charge carriers that stabilize atomic-scale filaments and, thus, the quantum conductance level<sup>38</sup>. The program-and-verify approach reported here does not aim to fine-tune the device resistance as in conventional programming schemes for in-memory computing<sup>39</sup>, but rather to nudge the device towards the quantum conductance operational regime while checking if the desired quantum conductance level is achieved. Note also that a similar program-and-verify approach is conventionally exploited for the practical realization of a d.c. voltage standard based on the Josephson effect to appropriately select the desired voltage level to be used as the reference standard (Supplementary Section 11)<sup>40</sup>. Figure 3a reports examples of devices programmed in air and at room temperature through the program-and-verify approach at  $G_1$  and  $G_2$  conductance values related to the  $G_0$  and  $2G_0$  quantum states, respectively. This program-and-verify approach makes it possible to achieve and sustain quantum conductance levels for up to 16,000 s (Extended Data Fig. 2). A comparison of the stability of quantum conductance values with previous works, including a comparison of device structures, switching mechanisms and programming approaches, is reported in Supplementary Section 12.

For the interlaboratory comparison, each laboratory performed a series of programming levels, and for each programmed level a time series of conductance measurements was carried out. For each time series, a mean value of the measurement conductance was evaluated. The repeatability was defined as the s.d. of the time series values (Methods and Supplementary Section 13). The reproducibility of the conductance value was defined as the s.d. of the mean values corresponding to each programming level. The uncertainty related to the measurement equipment was extracted from the instrument specifications and measurement conditions (Methods and Supplementary Section 14). The repeatability, reproducibility and uncertainty of the experimental set-up all contribute to the overall uncertainty. The complete set of measurements is reported in Extended Data Figs. 3 and 4. The validation of the programming methodology is detailed in Supplementary Section 15.

Figure 3b,c shows consistent repeatability in all laboratories in terms of the distribution of s.d. values for  $G_2$  and  $G_1$ , respectively. No significant trends were observed in the s.d. as a function of the measurement time interval, showing that the contribution of repeatability to the measurement result can be evaluated based on consecutive measurements performed at relatively short time intervals, <100 s (Extended Data Fig. 5). This means that, for practical applications, it

is possible to exploit the programmability of the memristive cell by on-demand programming it on the desired quantum conductance level when required without the need of long-term stability of the filament.

Figure 3d reports for each participant the mean value of the measured mean values and the corresponding s.d. of mean values of the considered quantum levels, and shows comparable reproducibility of programmed quantum levels in all the laboratories. As can be observed, the results for  $G_1$  and  $G_2$  are statistically consistent with expected  $G_0$  and  $2G_0$  quantum values and no s.d. values can be observed among the laboratories, revealing that laboratory-to-laboratory variability can be considered negligible compared with the variabilities related to the reproducibility of quantum steps. In addition, it can be observed that cycle-to-cycle variability dominates over device-to-device variability (Supplementary Section 16). The cycle-to-cycle variability can be attributed to the peculiar dynamic trajectories of nanofilament reconfiguration leading to slightly different atomic configurations near the quantum point contact, resulting in slight variations of quantum conductance levels around integer multiples of  $G_0$ , as analysed in a previous work<sup>41</sup>. Similarly, slight deviations from integer multiples of  $G_0$  were previously observed also in mechanically controllable break junctions<sup>42–44</sup>.

Figure 3e,f shows results for the estimation of the relative standard uncertainty components related to reproducibility, repeatability and measurement equipment of each partner for values of  $G_2$  and  $G_1$ , respectively. The figure shows that the component of uncertainty related to reproducibility is dominant. In terms of percentage, higher reproducibility and repeatability can be observed when considering values of  $G_2$  with respect to  $G_1$  (Fig. 3e,f). However, statistical results show no significant discrepancies in terms of reproducibility and repeatability between the  $G_2$  and  $G_1$  conductance states when considering absolute uncertainty component values (Extended Data Fig. 6). Although the contribution from the uncertainty related to the measurement equipment is comparable among all laboratories, it is not negligible.

### Memristive devices as a standard of resistance

A consensus value  $G_{\text{cons}}$  and its corresponding expanded uncertainty  $U(G_{\text{cons}})$  were established based on the participant's results for the investigated quantum conductance plateaus<sup>36,37</sup>. The aim of establishing a consensus value is to investigate a possible systematic deviation with respect to the exact quantization value. We choose as an estimate for  $G_{\text{cons}}$  the weighted mean of the values measured by participants<sup>35</sup>, while the combined uncertainty of the consensus value  $U(G_{\text{cons}})$  was

estimated based on the participant's combined uncertainties, which take into account all sources of uncertainties previously discussed and the coverage factor  $k$  calculated for a confidence level of 95% (see Methods for details). The normalized error  $E_n$  expresses the consistency of the results obtained by each participant with the consensus value<sup>35,37</sup> (see Methods for details). Mean values of quantum levels with the corresponding expanded uncertainties for all laboratories and normalized error with respect to the consensus value for  $G_1$  and  $G_2$  are reported in Fig. 4a,b, respectively. The evaluation of  $|E_n|$  values ( $\leq 1.0$  for all participants) shows that the measured conductance values belong to consistent datasets (Fig. 4a,b, right).  $G_{\text{cons}}$  was calculated to be  $(0.962 \pm 0.043)G_0$  and  $(2.012 \pm 0.051)G_0$  for  $G_1$  and  $G_2$ , respectively. It turns out that the error of the consensus values for  $G_1$  and  $G_2$  is  $-3.8\%$  and  $0.6\%$  with respect to the expected  $G_0$  and  $2G_0$  SI values, respectively. In summary, consensus values agree with SI values because their deviation from SI values is well covered by the expanded measurement uncertainty.

## Conclusions

In this work, we demonstrated an intrinsic and programmable resistance standard, based on quantum physics, that, at the cost of higher uncertainty with respect to conventional standards based on QHE, operates in air, at room temperature and can be miniaturized down to the nanometre scale. This standard has the significant advantage of low operating voltages (of the order of 10 mV) and low operating currents (of the order of 1  $\mu\text{A}$ ) during reading operations that are ideally suited for practical applications. It is worth mentioning that, even if electrochemical processes underlying filament formation/rupture are affected by temperature<sup>45</sup>, electronic transport phenomena leading to quantum conductance levels arising at the QPC is theoretically not affected by temperature and, in principle, traceability of the physical observable is not affected when the device is operating at different temperatures (Supplementary Section 17). All these characteristics enable the realization of an intrinsic quantum standard of electrical resistance/conductance that can be made available at the lower levels of the presently adopted traceability chain and can be directly implementable on chip, opening new opportunities for metrological traceability of electrical quantities. This makes possible its incorporation into any type of electronic measurement instrumentation, including multimeters, resistance bridges, temperature bridges, voltage dividers, voltage amplifiers, current amplifiers, temperature controllers, reference resistors in analogue-to-digital converters, etc. By means of autocalibration and autoadjustment processes, the on-chip standard allows the realization of electrical equipment with zero-chain traceability. In this context, it must be acknowledged also that a standard of resistance coupled with a voltage standard can enable the practical realization of a current standard according to the Bureau International des Poids et Mesures.

At the present stage, the deviations of quantum conductance states of memristive devices with respect to SI values are higher than the accuracy required by primary metrology achieved in NMs. Nevertheless, the availability of on-chip realization of the resistance standard can find applications (at lower levels of the traceability chain) where the periodical calibration of meters or sensors becomes inconvenient or impossible, and measurement traceability must be maintained over years or decades, in the spirit of the 'NMI-on-a-chip' paradigm. Examples lie in space applications, marine offshore environments, underground probes, sensing in remote locations, sensing in harsh environments and sensor networks.

For all these applications, several strategies can be exploited to improve the actual accuracy. From the device point-of view, further engineering of involved materials and stacked configurations combined with a refinement of the measurement protocol can be exploited to reduce the cycle-to-cycle variability, which is the dominant contribution to uncertainty. For example, the host matrix can be engineered to

promote electrochemical dynamics leading to only selected atomic configurations closely related to the  $G_0$  SI value. Further strategies to reduce stochastic effects related to cycle-to-cycle variability, to improve the stability of the filament and to reduce conductance drifts over extended timescales include (1) optimizing the sweep rate during electrochemical polishing, (2) combining electrochemical polishing with a partial RESET process to reduce stochastic effects related to the formation of a completely new filament during each SET/RESET operation, and (3) electropolishing of the filament in a small voltage window after programming (here the strategy is to vary not only the total voltage range, but also components in the positive and negative voltage sign and the sweep rate) (Supplementary Section 7). Moreover, for practical applications, the accuracy can be improved by using  $n$  independent devices in parallel to produce an average value of quantum levels that could improve variability by an order of  $\sqrt{n}$ . Similarly, a viable strategy includes also the mitigation of variability by mediating among multiple realizations of the same desired quantum conductance value, by leveraging the device programmability.

While the on-chip implementation of a resistance standard based on memristive cells necessarily requires additional circuitry to drive and control its operations, the complexity and costs of this control circuit (which can be easily miniaturized through conventional complementary metal-oxide-semiconductor technology) is significantly lower than the complexity and costs associated with the maintenance of the traceability chain and routine calibrations based on the conventional QHE-based resistance standard. In this context, we envision that the practical implementation of the self-calibration concept can be based on the artefact calibration paradigm<sup>46</sup>, where an on-chip memristive cell coupled with a mixed-signal application-specific integrated circuit that takes care of cell programming/reading could replace the external reference standard. For all these purposes, the circuit design can exploit the here-described behavioural model of memristive devices working in the quantum regime which can be implemented in conventional circuit simulators.

## Online content

Any methods, additional references, Nature Portfolio reporting summaries, source data, extended data, supplementary information, acknowledgements, peer review information; details of author contributions and competing interests; and statements of data and code availability are available at <https://doi.org/10.1038/s41565-025-02037-5>.

## References

1. *The International System of Units (SI)*, 9th edition, (Bureau International des Poids et Mesures, 2019); <https://www.bipm.org/en/publications/si-brochure>
2. Fischer, J. & Ullrich, J. The new system of units. *Nat. Phys.* **12**, 4–7 (2016).
3. *NIST on a Chip* (National Institute of Standards and Technology, accessed 3 October 2025); <https://www.nist.gov/noac>
4. Mise en pratique for the definition of the ampere and other electric units in the SI. *The International System of Units (SI)*, 9th edition (Bureau International des Poids et Mesures, 2019).
5. Milano, G. et al. Memristive devices for quantum metrology. *Adv. Quantum Technol.* **3**, 2000009 (2020).
6. Milano, G. et al. Quantum conductance in memristive devices: fundamentals, developments, and applications. *Adv. Mater.* **34**, 2201248 (2022).
7. Xue, W. et al. Recent advances of quantum conductance in memristors. *Adv. Electron. Mater.* **5**, 1800854 (2019).
8. Li, Y. et al. Conductance quantization in resistive random access memory. *Nanoscale Res. Lett.* **10**, 420 (2015).
9. Terabe, K., Hasegawa, T., Nakayama, T. & Aono, M. Quantized conductance atomic switch. *Nature* **433**, 47–50 (2005).

10. Tsuruoka, T., Hasegawa, T., Terabe, K. & Aono, M. Conductance quantization and synaptic behavior in a Ta<sub>2</sub>O<sub>5</sub>-based atomic switch. *Nanotechnology* **23**, 43 (2012).
11. Wagenaar, J. J. T., Morales-Masis, M. & Van Ruitenbeek, J. M. Observing quantized conductance steps in silver sulfide: two parallel resistive switching mechanisms. *J. Appl. Phys.* **111**, 014302 (2012).
12. Zhu, X. et al. Observation of conductance quantization in oxide-based resistive switching memory. *Adv. Mater.* **24**, 3941–3946 (2012).
13. Tappertzhofen, S., Valov, I. & Waser, R. Quantum conductance and switching kinetics of AgI-based microcrossbar cells. *Nanotechnology* **23**, 145703 (2012).
14. Long, S. et al. Quantum-size effects in hafnium-oxide resistive switching. *Appl. Phys. Lett.* **102**, 18 (2013).
15. Chen, C. et al. Conductance quantization in oxygen-anion-migration-based resistive switching memory devices. *Appl. Phys. Lett.* **103**, 043510 (2013).
16. Gao, S. et al. Conductance quantization in a Ag filament-based polymer resistive memory. *Nanotechnology* **24**, 335201 (2013).
17. Mehonic, A. et al. Quantum conductance in silicon oxide resistive memory devices. *Sci. Rep.* **3**, 2708 (2013).
18. Younis, A., Chu, D. & Li, S. Voltage sweep modulated conductance quantization in oxide nanocomposites. *J. Mater. Chem. C* **2**, 10291–10297 (2014).
19. Yi, W. et al. Quantized conductance coincides with state instability and excess noise in tantalum oxide memristors. *Nat. Commun.* **7**, 11142 (2016).
20. Nandakumar, S. R., Minvielle, M., Nagar, S., Dubourdieu, C. & Rajendran, B. A 250 mV Cu/SiO<sub>2</sub>/W memristor with half-integer quantum conductance states. *Nano Lett.* **16**, 1602–1608 (2016).
21. Krishnan, K., Muruganathan, M., Tsuruoka, T., Mizuta, H. & Aono, M. Highly reproducible and regulated conductance quantization in a polymer-based atomic switch. *Adv. Funct. Mater.* **27**, 1605104 (2017).
22. Banerjee, W. & Hwang, H. Quantized conduction device with 6-bit storage based on electrically controllable break junctions. *Adv. Electron. Mater.* **5**, 1900744 (2019).
23. Deswal, S., Malode, R. R., Kumar, A. & Kumar, A. Controlled inter-state switching between quantized conductance states in resistive devices for multilevel memory. *RSC Adv.* **9**, 9494–9499 (2019).
24. Chen, Q. et al. Controlled construction of atomic point contact with 16 quantized conductance states in oxide resistive switching memory. *ACS Appl. Electron. Mater.* **1**, 789–798 (2019).
25. Xue, W. et al. Controllable and stable quantized conductance states in a Pt/HfO<sub>x</sub>/ITO memristor. *Adv. Electron. Mater.* **6**, 1901055 (2020).
26. Zhao, X. et al. Natural acidic polysaccharide-based memristors for transient electronics: highly controllable quantized conductance for integrated memory and nonvolatile logic applications. *Adv. Mater.* **33**, 2104023 (2021).
27. Song, M. et al. Self-compliant threshold switching devices with high on/off ratio by control of quantized conductance in Ag filaments. *Nano Lett.* **23**, 2952–2957 (2023).
28. Maudet, F., Hammud, A., Wollgarten, M., Deshpande, V. & Dubourdieu, C. Insights on the variability of Cu filament formation in the SiO<sub>2</sub> electrolyte of quantized-conductance conductive bridge random access memory devices. *Nanotechnology* **34**, 245203 (2023).
29. *International Vocabulary of Metrology—Basic and General Concepts and Associated Terms (VIM)* (Bureau International des Poids et Mesures, 2012).
30. Rigosi, A. F. & Elmquist, R. E. The quantum Hall effect in the era of the new SI. *Semicond. Sci. Technol.* **34**, 093004 (2019).
31. Hartland, A. The quantum Hall effect and resistance standards. *Metrologia* **29**, 175–190 (1992).
32. Klitzing, K. V., Dorda, G. & Pepper, M. New method for high-accuracy determination of the fine-structure constant based on quantized Hall resistance. *Phys. Rev. Lett.* **45**, 494–497 (1980).
33. Patel, D. K. et al. A zero external magnetic field quantum standard of resistance at the 10<sup>-9</sup> level. *Nat. Electron.* <https://doi.org/10.1038/s41928-024-01295-w> (2024).
34. Wang, Z. et al. Resistive switching materials for information processing. *Nat. Rev. Mater.* **5**, 173–195 (2020).
35. Cox, M. G. The evaluation of key comparison data. *Metrologia* **39**, 589–595 (2002).
36. *ISO/IEC 17043: 2023-05, Ed. 2 Conformity Assessment—General Requirements for the Competence of Proficiency Testing Providers* (International Organization for Standardization, 2023).
37. *ISO 13528: 2022-08, Ed. 3—Statistical Methods for Use in Proficiency Testing by Interlaboratory Comparison* (International Organization for Standardization, 2022).
38. Kharlanov, O. G., Shvetsov, B. S., Rylkov, V. V. & Minnekhanov, A. A. Stability of quantized conductance levels in memristors with copper filaments: toward understanding the mechanisms of resistive switching. *Phys. Rev. Appl.* **17**, 054035 (2022).
39. Milo, V. et al. Accurate program/verify schemes of resistive switching memory (RRAM) for in-memory neural network circuits. *IEEE Trans. Electron Devices* **68**, 3832–3837 (2021).
40. Benz, S. P. & Hamilton, C. A. Application of the Josephson effect to voltage metrology. *Proc. IEEE* **92**, 1617–1629 (2004).
41. Milano, G. et al. Electrochemical rewiring through quantum conductance effects in single metallic memristive nanowires. *Nanoscale Horiz.* **9**, 416–426 (2024).
42. Krans, J. M. et al. One-atom point contacts. *Phys. Rev. B* **48**, 14721–14724 (1993).
43. Yanson, A. I., Bollinger, G. R., van den Brom, H. E., Agraït, N. & van Ruitenbeek, J. M. Formation and manipulation of a metallic wire of single gold atoms. *Nature* **395**, 783–785 (1998).
44. Rodrigues, V., Fuhrer, T. & Ugarte, D. Signature of atomic structure in the quantum conductance of gold nanowires. *Phys. Rev. Lett.* **85**, 4124–4127 (2000).
45. Menzel, S., Tappertzhofen, S., Waser, R. & Valov, I. Switching kinetics of electrochemical metallization memory cells. *Phys. Chem. Chem. Phys.* **15**, 6945 (2013).
46. Rietveld, G. Artifact calibration—the role of software in metrology. In *National Conference of Standard Laboratories (NCSL) Workshop and Symposium, Monterey, CA 315–322* (NCSLI, 1996).

**Publisher's note** Springer Nature remains neutral with regard to jurisdictional claims in published maps and institutional affiliations.

**Open Access** This article is licensed under a Creative Commons Attribution 4.0 International License, which permits use, sharing, adaptation, distribution and reproduction in any medium or format, as long as you give appropriate credit to the original author(s) and the source, provide a link to the Creative Commons licence, and indicate if changes were made. The images or other third party material in this article are included in the article's Creative Commons licence, unless indicated otherwise in a credit line to the material. If material is not included in the article's Creative Commons licence and your intended use is not permitted by statutory regulation or exceeds the permitted use, you will need to obtain permission directly from the copyright holder. To view a copy of this licence, visit <http://creativecommons.org/licenses/by/4.0/>.

© The Author(s) 2025

## Methods

### Device fabrication

Memristive devices were fabricated by sandwiching a SiO<sub>2</sub> insulator in between a platinum bottom electrode and a silver top electrode. The choice of silver as the top electrode is based on its electrochemical activity which allows dissolution of silver atoms and migration of Ag<sup>+</sup> ions at lower voltages compared to other noble metals, while platinum was chosen as the counter-electrode because it is electrochemically inert (details on the selection of materials and device configuration can be found in Supplementary Section 5). The pad structure devices were fabricated on a thermally oxidized silicon substrate starting with the d.c. magnetron sputtering deposition (power, 200 W) of a TiO<sub>2</sub> (10 nm) adhesion layer and a platinum (100 nm) bottom electrode. The homogeneous SiO<sub>2</sub> film (20 nm) with a purity of 8N was deposited by radiofrequency (RF) magnetron sputtering with a sputtering power of 150 W in a processing gas mixture of 9 sccm argon and 1 sccm oxygen at 150 °C. Note that the choice of the 8 N SiO<sub>2</sub> matrix is related to the very low level of impurities, a potential disturbing factor for achieving controlled conductance states. Also, the resulting SiO<sub>2</sub> is rather stoichiometric and chemical and physical interactions with silver are not thermodynamically favourable. Following switching layer deposition, feature sizes of 50 × 50 μm<sup>2</sup> were patterned by negative photolithography. Then, the Ag (20 nm) active top electrode was deposited by e-beam evaporation with a deposition rate of 0.01 nm s<sup>-1</sup>, followed by a d.c.-sputtered platinum (50 nm) capping layer. The role of the capping layer is to prevent degradation of the silver active electrode over time as required for long-term use of the device. A standard lift-off process was utilized for the final cleaning of devices, obtaining an Ag/SiO<sub>2</sub>/Pt cell with a top electrode size of 50 × 50 μm<sup>2</sup>.

### Device modelling

Departing from the experimental observation of well-defined conductance jumps and states, we model the RESET transition (the SET transition is also considered for generality) as a random generation of events related to the destruction of single quantum mode channels with conductance ~G<sub>0</sub>. This is a stochastic version of a continuous behavioural compact model<sup>47</sup> which has been successfully applied to memristors with different material systems, different switching modes (bipolar, unipolar, complementary and threshold switching) and for the SPICE simulation of neuromorphic circuits. The stochastic version of the model presented here was recently applied to valence change memory devices which show variability, but not quantum conductance jumps<sup>48</sup>.

The stochastic resistive switching model follows Chua's approach<sup>49</sup> to memristors and is based on two equations, one for the current and one for the internal memory variable. In our case, the memory state variable is the number of conducting channels, *n<sub>ch</sub>*, each of these channels contributing ~G<sub>0</sub> to the filament conductance. In a naive interpretation, each of these channels can be considered either as 'atomic chains' or as 'quantized quantum transport modes' in the filament constriction. This is a simple implementation of the Landauer theory for ballistic transport through an atomic-size constriction<sup>50</sup>. We consider that the SET/RESET transitions occur by successive discrete conductance jumps (events) corresponding to the creation/destruction of single conduction channels. For simplicity, we assume that each switching event increases or decreases the conductance by the same amount. However, this might not be completely realistic because several channels can be created/destroyed at the same time. During the RESET transition, we will consider that each jump is |Δ*G*| = G<sub>0</sub>. Given the experimental results, we impose that the first SET event is abrupt so that the device reaches the compliance limit in a single conductance jump. The creation/destruction of single channels will occur at random times during the application of the external electrical signal (voltage/current). For the sake of generality, we limit the number of channels to *n<sub>max</sub>*. This parameter is related to the maximum area of the filament

created during electroforming. Under these conditions, the proposed memory equation is:

$$\frac{dn_{ch}}{dt} = \frac{n_{max} - n_{ch}}{\tau_S} - \frac{n_{ch}}{\tau_R} \quad (1)$$

where the two terms of the right-hand side (RHS) represent the SET and RESET transitions, and *τ<sub>S</sub>* and *τ<sub>R</sub>* are the SET and RESET characteristic times, respectively. Because the SET transition resembles the dielectric breakdown process and is strongly accelerated by the electric field, an exponential voltage dependence for *τ<sub>S</sub>* is assumed:

$$\tau_S(V) = \tau_{S0} \exp[-\gamma_S(V - IR_S)] \quad (2)$$

where *γ<sub>S</sub>* is the acceleration factor, *τ<sub>S0</sub>* is the time scale prefactor, *I* is current, *V* is voltage and *R<sub>S</sub>* is the series resistance. On the other hand, consistently with the electropolishing interpretation, the RESET transition is assumed to be controlled by the oxidation/reduction dynamics and/or by the out-diffusion of species to the filament surroundings. Because both processes are strongly accelerated by temperature, we neglect voltage acceleration (as discussed within the electropolishing interpretation) and we only consider the local temperature rise related to the power dissipated in the filament, *P* = *I*(*V* - *IR<sub>S</sub>*). Assuming an Arrhenius temperature dependence as a first-order approximation, the characteristic RESET time, *τ<sub>R</sub>*, can be described as:

$$\tau_R(V) = \tau_{R0} \exp\left[\frac{E_a}{K_B(T + R_{TH}P)}\right] \quad (3)$$

where *τ<sub>R0</sub>* is the RESET scale prefactor, *E<sub>a</sub>* is the activation energy, *K<sub>B</sub>* is the Boltzmann constant, *T* is the external temperature and *R<sub>TH</sub>* is the thermal resistance. The thermal resistance has been described in the literature in terms of two parallel paths for heat evacuation<sup>51</sup>. The longitudinal thermal resistance, *R<sub>L</sub>*, corresponding to heat transport along the channel (related to the electrical conductivity) and the transverse resistance, *R<sub>T</sub>*, associated with heat transport towards the surrounding material. The latter is independent of the filament size to the first order, while *R<sub>L</sub>* is inversely proportional to the filament area, represented here by *n<sub>ch</sub>*, which is proportional to the area. Thus, we can write *R<sub>L</sub>* = *K<sub>L</sub>*/*n<sub>ch</sub>*, where *K<sub>L</sub>* is a constant. The total thermal resistance is given by the parallel combination of *R<sub>L</sub>* and *R<sub>T</sub>*, so that *R<sub>TH</sub>* = (*K<sub>L</sub>R<sub>T</sub>*) / (*n<sub>ch</sub>R<sub>T</sub>* + *K<sub>L</sub>*). It is worth remarking that we included only description of thermal dissipation with a phenomenological approach based on macroscopic parameters such as thermal resistances. While in principle quantum thermal effects cannot be ruled out, experimental works pointed out that these effects only become not negligible in the low-temperature regime<sup>52</sup>, that is, far away from the room temperature conditions of our work.

Because *τ<sub>S</sub>* has a strong exponential dependence on voltage, it emerges that *τ<sub>S</sub>* << *τ<sub>R</sub>* for positive voltages and *τ<sub>S</sub>* >> *τ<sub>R</sub>* for negative voltages. Because of this, we can separately consider the SET and RESET transitions with two separate differential equations. One for the SET:

$$\frac{dn_{ch}}{dt} = \frac{n_{max} - n_{ch}}{\tau_S} \quad (4)$$

And one for the RESET:

$$\frac{dn_{ch}}{dt} = -\frac{n_{ch}}{\tau_R} \quad (5)$$

As far as the current is concerned, we have considered:

$$I(V) = \frac{n_{ch}G_0}{1 + n_{ch}G_0R_S} V + I_B \sinh[\eta(V - IR_S)] \quad (6)$$

where  $\eta$  is a shape parameter related to the potential barrier at the constriction when there are no conducting channels. The first term corresponds to the conduction through the  $n_{\text{ch}}$  channels, and the second to the background tunnelling regime, that is, when the filament has a gap. Although the considered voltage dependence of the background current can be discussed, this is not relevant to our work because we focus on situations where there is at least one conducting channel with a conductance which is generally much larger than that of the background. Finally, notice that  $n_{\text{ch}}$  couples the current and memory equations.

For the generation of random events, we follow an ‘on-the-fly’ method. If the number of events (conductance jumps) is  $n(t)$ , the event generation rate is  $\lambda(t) = dn(t)/dt$ . During the SET transition,  $n_{\text{ch}} = n(t)$  so that  $\lambda(t) = dn_{\text{ch}}/dt$ , while during RESET  $n_{\text{ch}} = n_{\text{max}} - n(t)$ , so that  $\lambda(t) = -dn_{\text{ch}}/dt$ . Thus, the event generation rates can be obtained from equations (4) and (5) so that  $\lambda_{\text{S}} = (n_{\text{max}} - n_{\text{ch}})/\tau_{\text{S}}$  and  $\lambda_{\text{R}} = n_{\text{ch}}/\tau_{\text{R}}$  during SET and RESET, respectively. Since  $n_{\text{max}} > n_{\text{ch}}$  at any time, both generation rates are always positive as they must be. For the RESET transition, we will depart from an initial number of channels,  $n_{\text{init}}$ , which are the ones generated during the previous SET transition.

The events are generated with a random number  $u$  uniformly distributed between 0 and 1 along the simulation time. The simulation time is discretized in steps  $\Delta t$  which are small enough so that  $\lambda(t)$  can be assumed to be constant during  $\Delta t$ . It can be shown that under these conditions, the random time to a subsequent event at time  $t$  is  $\Delta t_u = -\ln(u)/\lambda(t)$ . During the simulation, if  $\Delta t_u < \Delta t$  an event is generated at time  $t$ , otherwise, the event is rejected. Details on modelling are discussed in Supplementary Section 9.

### Interlaboratory comparison

An interlaboratory comparison involving six participants was carried out for the electrical characterization of quantum conductance levels in memristive devices, with the aim of testing the intrinsic standard of electrical conductance (or resistance) and for evaluating laboratory-to-laboratory variability. For this purpose, samples assumed to be identical were distributed among participants and a common measurement protocol was defined. The participants were the following institutions: Istituto Nazionale di Ricerca Metrologica (Italian Institute of Metrology, NMI 1), Instituto Português da Qualidade (Portuguese Institute of Metrology, NMI 2), Türkiye Bilimsel ve Teknolojik Arastırma Kurumu (Turkish Institute of Metrology, NMI 3), Forschungszentrum Juelich GmbH (LAB 1), Fundación IMDEA Nanociencia (LAB 2) and Politecnico di Torino (LAB 3).

### Measurement protocol

The equivalence of the measurements across the different laboratories was ensured by establishing and agreeing a measurement protocol that defines standardized measurement conditions to program, accept and stabilize the quantum conductance level, and defines the methodology to measure its conductance value under steady conditions (an example of the device programming methodology is reported in Extended Data Fig. 1). The generation of the quantum conductance states is achieved by running sequential SET/RESET cycles where an applied voltage to the two terminals of the device is swept between +1.5 V and -0.9 V. The positive part of the sweep (SET cycle) has a sweep rate of 96 mV s<sup>-1</sup> (voltage steps of 50 mV). The negative sweep (RESET cycle) has a slower sweep rate of 2 mV s<sup>-1</sup> (voltage steps of 1 mV). The current compliance was established as 500  $\mu$ A and 10 mA for the positive and negative cycles, respectively. The voltage at the terminals of the device and the current that flows through it are continuously measured over SET/RESET cycles, and the corresponding conductance state is obtained for each applied voltage step. The formation of the quantum conductance steps during the RESET is continuously verified and a criterion to detect and accept  $G_1$  and  $G_2$  conductance states related to  $G_0$  and  $2G_0$  quantum values, respectively, was established.

If the last five consecutive measurements of the conductance state lay within either  $G_0 \pm 0.5G_0$  or  $2G_0 \pm 0.5G_0$  (censoring interval), the sweep RESET cycle is interrupted, and a continuous read voltage of 10 mV is applied. The measurement of the step conductance value starts under this fixed applied control voltage and continues as long as it remains in the intervals  $[0.5G_0; 1.5G_0]$  or  $[1.5G_0; 2.5G_0]$ . The measurements were made at room temperature and under normal environmental conditions. The equipment used was a source meter (different equipment was used by the participants, as detailed in Supplementary Section 14) in autorange mode. The above-described methodology makes it possible to deal with the stochasticity of the conductive filament formation process establishing an initial limit to the variability around the nominal values of the desired quantum conductance steps (the validation of this programming methodology is discussed in Supplementary Section 15). Note that all measurements not strictly following the established comparison protocol were not considered for the interlaboratory comparison.

### Evaluation of results and uncertainty budget

The evaluation of the average value and the variability of the programmed quantum steps was made from the observation of the measurements taken under repeatability and reproducibility conditions (described in appendix 2 of ref. 4). Here, repeatability conditions are understood as measurements of a specific device taken consecutively, while reproducibility is considered as the variability of the measurements taken from cycle-to-cycle operation of a specific device and programmed state as well as from device-to-device operations.

For each participant,  $j$ , the arithmetic mean and the experimental standard deviation were calculated for each series  $i$  of  $n_i$  values:

$$\bar{G}_{j,i} = \frac{1}{n_i} \sum_{a=1}^{n_i} G_{i,a} \quad (7)$$

$$s_{j,i} = \sqrt{\frac{1}{n_i - 1} \sum_{a=1}^{n_i} (G_{i,a} - \bar{G}_{j,i})^2} \quad (8)$$

The s.d. given by equation (8) is an estimate of the repeatability<sup>53,54</sup> associated with series  $i$  of a programmed quantum conductance state measured by participant  $j$ . Only series with a minimum of 30 consecutive values and limited to a maximum of 100 values were considered as a fixed condition in this data evaluation (Supplementary Section 13). As each participant measured  $N_j$  series and there are series with different numbers of values, a polled standard deviation<sup>55</sup>  $s_{p,j}^2$  is calculated based on the following equation for its variance:

$$s_{p,j}^2 = \frac{\sum_{i=1}^{N_j} (n_i - 1) \times s_{j,i}^2}{\sum_{i=1}^{N_j} (n_i - 1)} \quad (9)$$

$s_{p,j}$  is therefore a weighted average of the  $N_j$  s.d. where the number of degrees of freedom ( $n_i - 1$ ) is the weight of each series.

For each participant, an average of the mean values obtained from the  $N_j$  series and the experimental s.d. is calculated as:

$$\bar{G}_j = \frac{1}{N_j} \sum_{i=1}^{N_j} \bar{G}_{j,i} \quad (10)$$

$$S_j = \sqrt{\frac{1}{N_j - 1} \sum_{i=1}^{N_j} (\bar{G}_{j,i} - \bar{G}_j)^2} \quad (11)$$

The evaluation of the reproducibility of the programmed quantum conductance steps was based on the s.d.<sup>53,54</sup> given by equation (11). Because the values obtained by each participant for each step are from

different cycles and different devices, the reproducibility obtained is the result of cycle-to-cycle and device-to-device variability.

The measurement of quantum conductance states associated with each participant is expressed by the following measurement equation:

$$G_j = \bar{G}_j + S_j + s_{p,j} + e_j \quad (12)$$

where  $\bar{G}_j$  is the mean value calculated by participant  $j$ ,  $S_j$  is the related experimental s.d. according to equations (10) and (11),  $s_{p,j}$  is the repeatability of the measurements according to equation (9), and  $e_j$  is the error related to the accuracy of the measurement equipment used. It is assumed that these input variables are statistically random variables where  $S_j$ ,  $s_{p,j}$  and  $e_j$  have an expectation value equal to zero and a s.d. estimated based on the experimental values presented before ( $S_j$  and  $s_{p,j}$ ) and in the manufacturing specifications of the equipment used (for  $e_j$ ). Note that random effects, including cycle-to-cycle variability but also variations related to small variations in the room temperature, humidity levels or even small fluctuations from the measurement set-up, are included in the estimation of the uncertainty component of the quantities  $S_j$  and  $s_{p,j}$ , even if each specific contribution has not been disentangled.

The measuring uncertainty of  $G_j$  can be estimated by applying the law of propagation of uncertainties<sup>35</sup> to equation (12):

$$u^2(G_j) = u^2(S_j) + u^2(s_{p,j}) + u^2(e_j) \quad (13)$$

where  $u^2(x)$  is the variance (square of standard uncertainty) associated with the variable  $x$  and  $u^2(G_j)$  is the square of the combined uncertainty of  $G_j$ .

The standard uncertainties of  $S_j$  and  $s_{p,j}$  are estimated by the corresponding s.d. of the mean:

$$u(S_j) = \frac{1}{\sqrt{N_j}} S_j \quad (14)$$

$$u(s_{p,j}) = \frac{1}{\sqrt{\sum_{i=1}^{N_j} (n_i) / N_j}} s_{p,j} \quad (15)$$

The relative standard uncertainty of  $e_j$  is calculated from the combined relative uncertainty of the measurement of the voltage,  $u_r^2(U)$ , and current,  $u_r^2(I)$ :

$$u_r(e) = \sqrt{u_r^2(U) + u_r^2(I)} \quad (16)$$

The relative uncertainties of the measured voltage  $U$  and current  $I$  are estimated assuming a rectangular probability distribution for the voltage and the current measuring error with the plus/minus limits given by the manufacturing specifications of the equipment, usually identified as 'accuracy' (Supplementary Section 14):

$$u_r(U) = \frac{1}{\sqrt{3}} \frac{U_{\text{accuracy}}}{U} \quad (17)$$

$$u_r(I) = \frac{1}{\sqrt{3}} \frac{I_{\text{accuracy}}}{I} \quad (18)$$

Following the international recommendation to express the final measuring uncertainty with a coverage probability of approximately 95%<sup>36,37</sup>, the expanded uncertainty  $U(G_j)$  is calculated following the equation:

$$U(G_j) = k \times u(G_j) \quad (19)$$

where  $k$  is the coverage factor calculated according to annex G of ref. 55.

## Evaluation of consensus value

The evaluation of the results achieved by the participants was done by comparing individual results with a consensus value<sup>36,37</sup>. The consensus value is established based on all results from the participants<sup>37</sup>, using a weighted average of their values<sup>35</sup>:

$$G_{\text{cons}} = \left( \sum_{j=1}^6 w_j \times G_j \right) / \left( \sum_{j=1}^6 w_j \right) \quad (20)$$

where the weighting factors are given by:

$$w_j = 1/u^2(G_j) \quad (21)$$

The combined uncertainty of the consensus value is estimated based on the participant uncertainties as follows:

$$u(G_{\text{cons}}) = \sqrt{1 / \sum_{j=1}^6 w_j} \quad (22)$$

And the related expanded uncertainty is given assuming a coverage factor  $k = 2$  (ref. 35):

$$U(G_{\text{cons}}) = 2 \times u(G_{\text{cons}}) \quad (23)$$

To identify an overall consistency of the results produced by this approach, a chi-square test was applied to the input values<sup>35</sup>:

$$\chi_{\text{obs}}^2 = \sum_{j=1}^n \left[ (G_j - G_{\text{cons}})^2 / u^2(G_j) \right] \quad (24)$$

The result of the test is considered to fail if  $\text{Pr} \{ \chi^2(v) > \chi_{\text{obs}}^2 \} < 0.05$  where  $\text{Pr}$  is the 'probability of',  $\chi^2(v)$  is the expected theoretical value of a chi-squared distribution for  $v$ , and  $v$  is the degrees of freedom, which is the number of input values  $n$  minus 1 (in this case, 5). If the consistency check does not fail, then  $G_{\text{cons}}$  can be accepted as the consensus value and  $U(G_{\text{cons}})$  can be accepted as its expanded uncertainty. Values obtained for the interlaboratory comparison were  $\chi_{\text{obs}}^2 = 6.3$  and  $\chi^2(5) = 11.1$ . As  $\chi_{\text{obs}}^2 \leq \chi^2(5; 0.05)$ , the consistency of the participant's values and the calculated consensus value was demonstrated, thus the obtained  $G_{\text{cons}}$  is the consensus value and  $U(G_{\text{cons}})$  is its expanded uncertainty.

To qualify the result of each participant related to the consensus value, the normalized error<sup>35,37</sup>,  $E_{n,j}$ , was calculated by:

$$E_{n,j} = (G_j - G_{\text{cons}}) / \sqrt{U^2(G_j) - U^2(G_{\text{cons}})} \quad (25)$$

The value of  $E_{n,j}$  has the following meaning: if  $|E_{n,j}| \leq 1.0$ , the result is consistent (passed); if  $|E_{n,j}| > 1.0$ , the result is inconsistent (failed). For all participants, results were observed to be consistent with the established consensus value. Based on statistical analysis, higher values of  $|E_{n,j}|$  (even if always  $\leq 1.0$ ) cannot be ascribed to eventual systematic errors affecting the measurement that are not being adequately corrected or considered in the evaluation of measurement uncertainty.

## Data availability

The data that support the findings of this study are available via Zenodo at <https://doi.org/10.5281/zenodo.16788655> (ref. 58). All other data are available from the corresponding authors.

## References

- Miranda, E. & Sune, J. Memristive state equation for bipolar resistive switching devices based on a dynamic balance model and its equivalent circuit representation. *IEEE Trans. Nanotechnol.* **19**, 837–840 (2020).

48. Suñé, J., Bargalló-González, M., Saludes, M., Campabadal, F. & Miranda, E. Event-driven stochastic compact model for resistive switching devices. *IEEE Trans. Electron Devices* **71**, 4649–4654 (2024).
49. Chua, L. Resistance switching memories are memristors. *Appl. Phys. A* **102**, 765–783 (2011).
50. Landauer, R. Spatial variation of currents and fields due to localized scatterers in metallic conduction. *IBM J. Res. Dev.* **1**, 223–231 (1957).
51. Russo, U., Ielmini, D., Cagli, C. & Lacaita, A. L. Filament conduction and reset mechanism in NiO-based resistive-switching memory (RRAM) devices. *IEEE Trans. Electron Devices* **56**, 186–192 (2009).
52. Pekola, J. P. & Karimi, B. Colloquium: Quantum heat transport in condensed matter systems. *Rev. Mod. Phys.* **93**, 041001 (2021).
53. *ISO 5725-1: 2023-07—Accuracy (Trueness and Precision) of Measurement Methods and Results—Part 1: General Principles and Definitions* (International Organization for Standardization, 2023).
54. *ISO 3534-2: 2006—Statistics—Vocabulary and Symbols—Part 2: Applied Statistics* (International Organization for Standardization, 2006).
55. *JCGM 100: 2008—Evaluation of Measurement Data—Guide to the Expression of Uncertainty in Measurement* (Bureau International des Poids et Mesures, 2008).
56. *ILAC-G17:01/2021—ILAC Guidelines for Measurement Uncertainty in Testing* (International Laboratory Accreditation Cooperation, 2021).
57. *ILAC-P14:09/2020—ILAC Policy for Measurement Uncertainty in Calibration* (International Laboratory Accreditation Cooperation, 2020).
58. Milano, G. et al. A quantum resistance memristor for an intrinsically traceable International System of Units standard - Dataset. *Zenodo* <https://doi.org/10.5281/zenodo.16788655> (2025).

## Acknowledgements

This work was supported by the European project MEMQuD, code 20FUN06. This project (EMPIR 20FUN06 MEMQuD) has received funding from the European Metrology Programme for Innovation and

Research (EMPIR) cofinanced by the participating states and from the European Union's Horizon 2020 research and innovation programme.

## Author contributions

G.M., V.C. and I.V. generated the idea. G.M., V.C. and I.V. supported by X.Z. and F.M. designed the experiments. X.Z. designed and performed device fabrication. G.M., V.C. and F.M. supported by X.Z. developed the measurement protocol for the interlaboratory comparison. X.Z., F.M., G.L., G.C., I.O. and V.C. performed electrical measurements. V.C., J.S. and G.M. performed data analysis. J.S. and E.M. developed the model. G.M., L.B., O.B., L.C., N.D.L., I.G., D.G., I.K., M.M., E.M., L.R., C.R., J.S., V.C. and I.V. supervised the research.

## Funding

Open access funding provided by Forschungszentrum Jülich GmbH.

## Competing interests

The authors declare no competing interests.

## Additional information

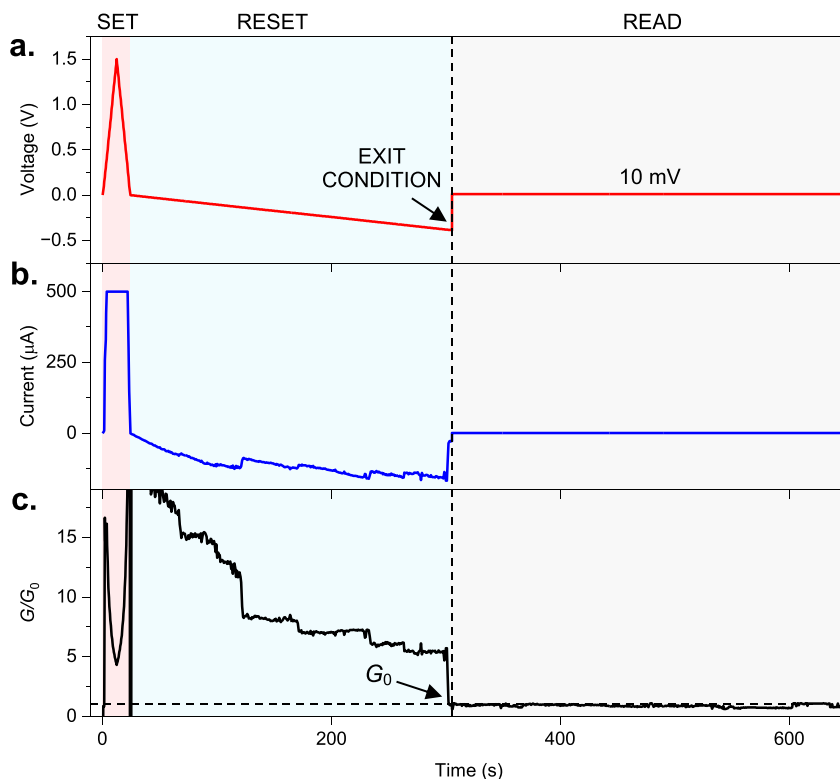
**Extended data** is available for this paper at <https://doi.org/10.1038/s41565-025-02037-5>.

**Supplementary information** The online version contains supplementary material available at <https://doi.org/10.1038/s41565-025-02037-5>.

**Correspondence and requests for materials** should be addressed to Gianluca Milano, Vitor Cabral or Ilia Valov.

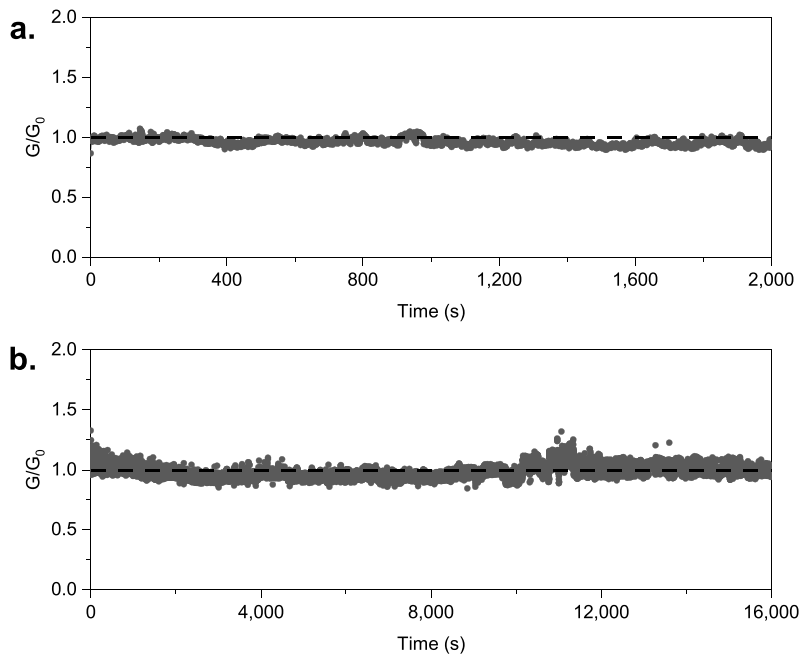
**Peer review information** *Nature Nanotechnology* thanks Run-Wei Li and the other, anonymous, reviewer(s) for their contribution to the peer review of this work.

**Reprints and permissions information** is available at [www.nature.com/reprints](http://www.nature.com/reprints).



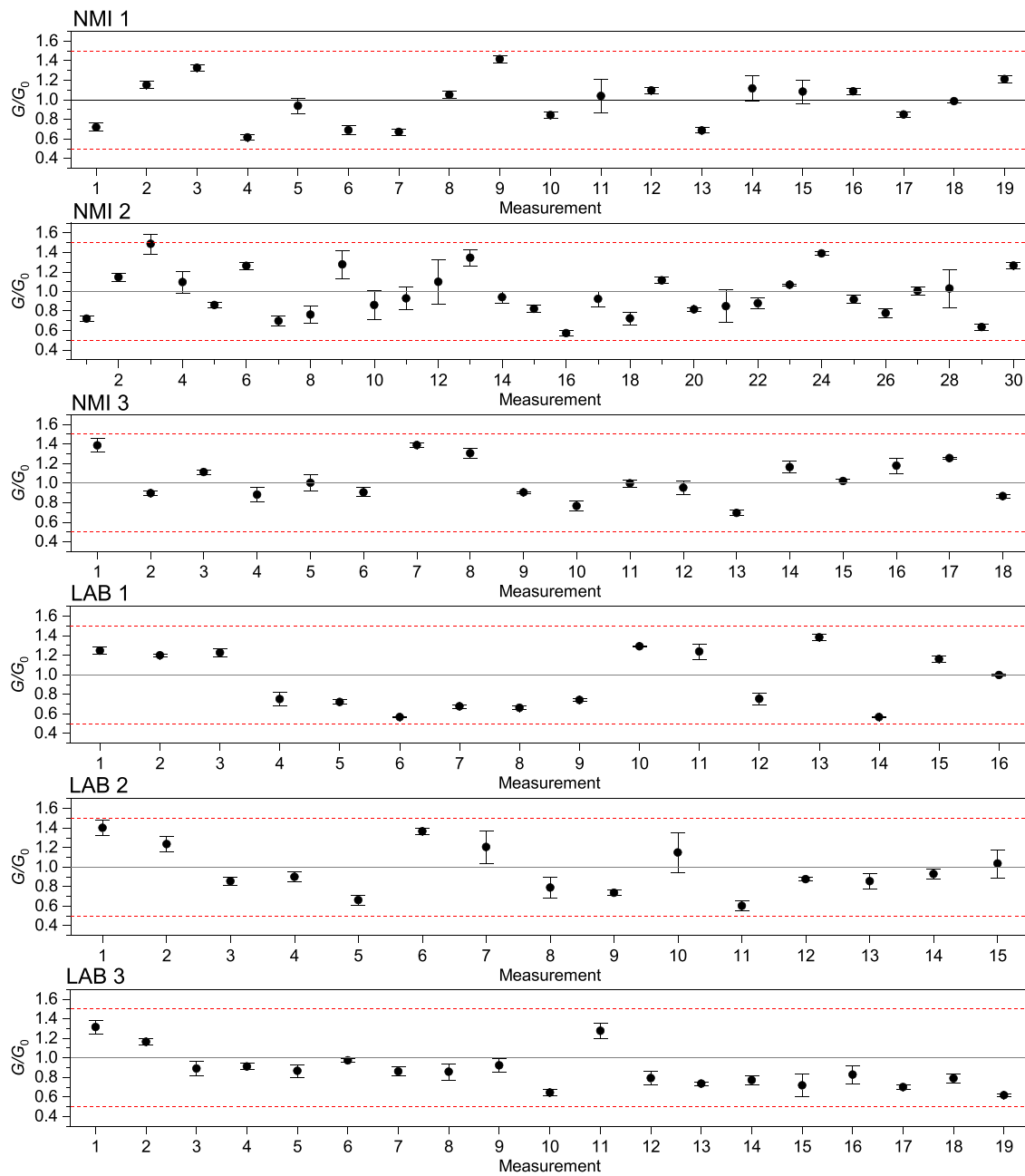
**Extended Data Fig. 1 | Program-and-verify approach to program the device to the desired quantum conductance levels.** This approach consists in the following steps: *i*) SET of the device through a positive voltage sweep cycles in between 0 and 1.5 V (sweep rate of  $96 \text{ mV s}^{-1}$ , compliance current of  $500 \mu\text{A}$  externally controlled to avoid hard breakdown of the device) (red shadowed region); *ii*) RESET the device through a negative slow voltage sweep ( $2 \text{ mV s}^{-1}$ ) from 0 down to  $-0.9 \text{ V}$  to achieve a step-like decrease of device conductance due to quantum conductance effects (blue shadowed region); *iii*) READ of the desired

quantum level with a continuous constant voltage, if the exit condition has been satisfied during the RESET step, the RESET cycle is interrupted and the control changes to a continuously positive read voltage of  $10 \text{ mV}$  (grey shadowed region). The exit condition is considered satisfied if the device exhibits during the time series at least 5 consecutive conductance measurements in the desired quantum level  $\pm 0.5G_0$ . Note that the device is continuously cycled until the desired quantum level has been obtained. **a**, Programming voltage; **b**, measured current; **c**, the device conductance.

**Extended Data Fig. 2 | Stability of programmed quantum conductance levels.**

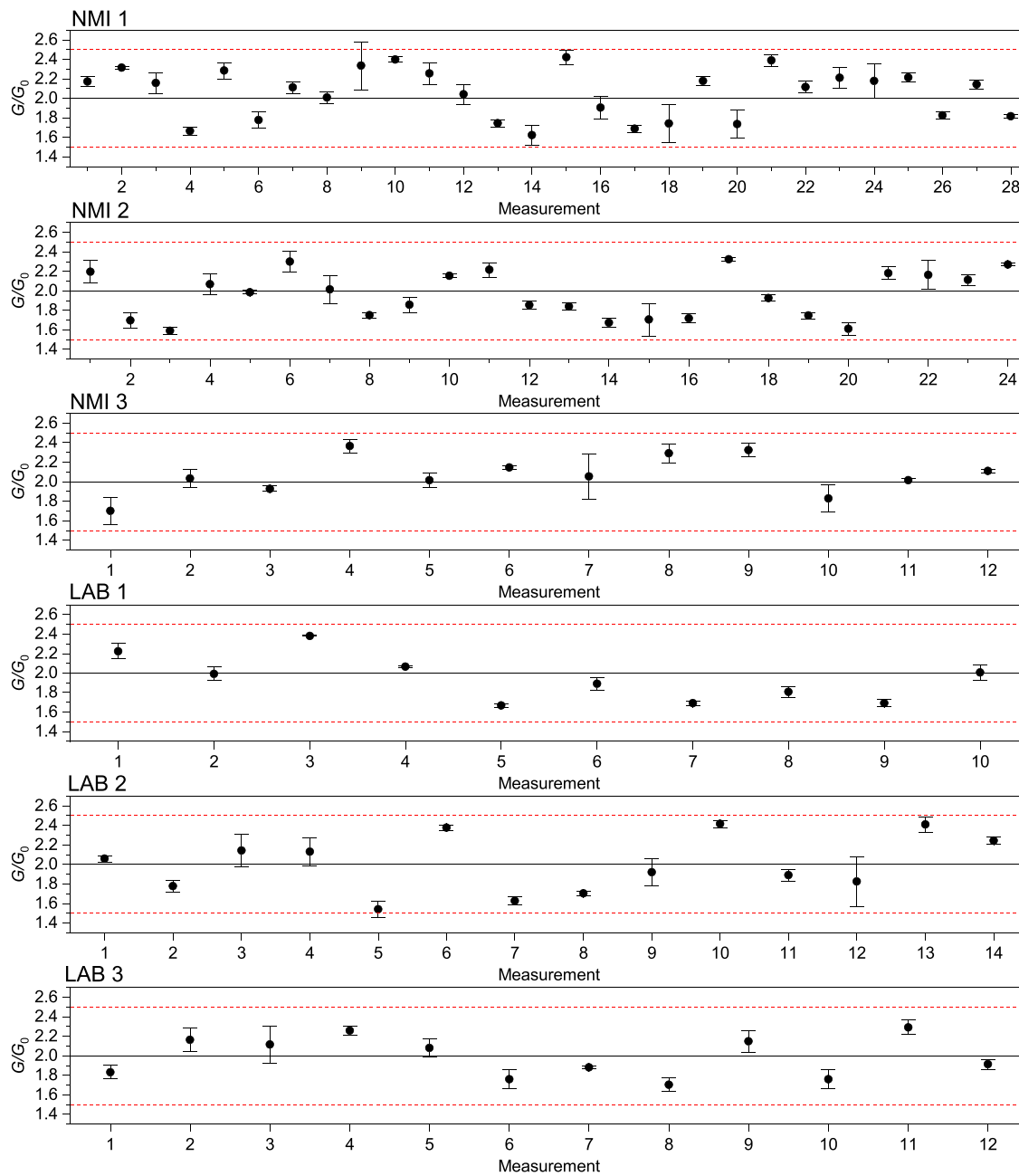
**a.** Example of a quantum conductance level measured at NMI 1 observed to be stable up to 2000 s under constant voltage reading of 10 mV (initial data are reported in Fig. 3a). **b.** Example of a quantum conductance level measured at NMI 3 observed to be stable up to 16000 s under constant reading voltage of 10 mV.

Dashed lines represent the  $G_0$  reference value. Quantum conductance levels in panels a and b have been obtained through the program-and-verify approach, with negative voltage sweep for gradual RESET of  $2 \text{ mV s}^{-1}$  and  $80 \text{ mV s}^{-1}$ , respectively.



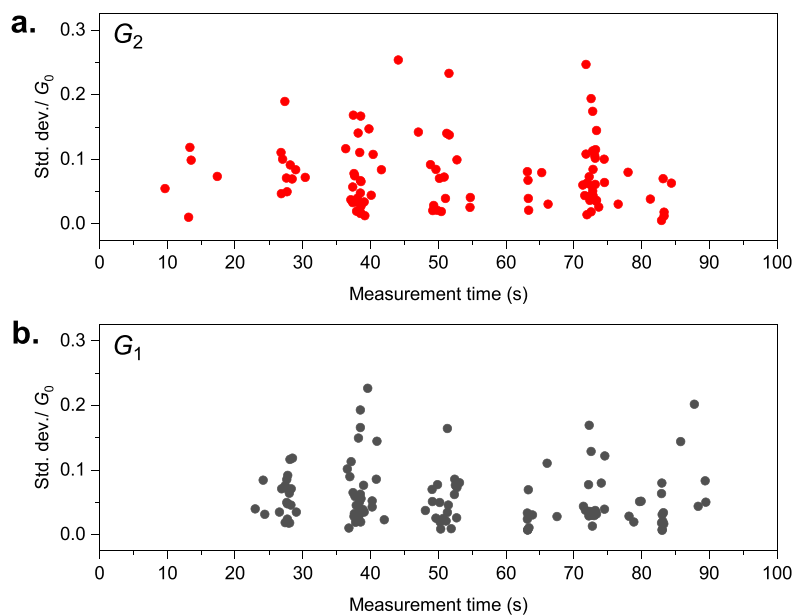
**Extended Data Fig. 3 |  $G_1$  conductance plateaus related to the  $G_0$  quantum level from the interlaboratory comparison.** Each data point is the mean value and error bar is the standard deviation representing the repeatability evaluated

over  $n$  (30 to 100) repeated measurements of the same conductance value. Red dashed lines represent boundaries of the exit condition of the program-and-verify approach, while grey line represents the  $G_0$  reference line.



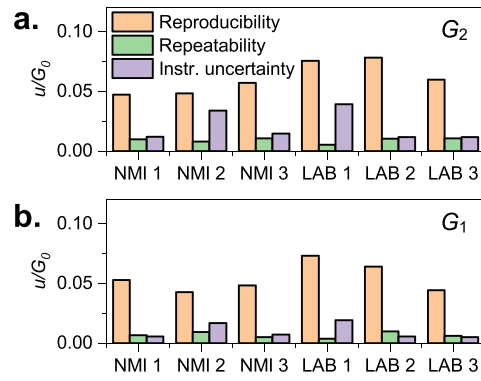
**Extended Data Fig. 4 |  $G_2$  conductance plateaus related to the  $2G_0$  quantum level from the interlaboratory comparison.** Each data point is the mean value and error bar is the standard deviation representing the repeatability evaluated

over  $n$  (30 to 100) repeated measurements of the same conductance value. Red dashed lines represent boundaries of the exit condition of the program-and-verify approach, while grey line represents the  $2G_0$  reference line.



**Extended Data Fig. 5 | Measurement repeatability and time interval of consecutive measurements.** Repeatability in terms of the standard deviation of  $n$  consecutive measurements evaluated for conductance levels related to  $2G_0$  (panel a.) and to  $G_0$  (panel b.), for a measurement time up to 100 s. Each point has been evaluated by programming the device to a desired programmed quantum level and then evaluating the standard deviation of  $n$  (30 to 100) consecutive measurements of the conductance step. Graphs have been obtained through aggregated data analysis of results obtained by different labs in the interlaboratory comparison. In case of equal number of consecutive

measurements, different measurement time intervals arise from different sample rates of measurement arising from different experimental equipment and their configuration parameters (for example NPLC – Number of Power Line Cycles, Filter, etc) exploited for the interlaboratory comparison. As can be observed, no significant trend can be observed in the standard deviation as a function of the measurement time interval, suggesting that the repeatability can be evaluated based on consecutive measurements performed on a small-time interval.



**Extended Data Fig. 6 | Uncertainty budget – absolute values.** Absolute standard uncertainty components of  $G_2$  (panel a.) and  $G_1$  (panel b.) related to reproducibility, repeatability, and measurement equipment for each participant.